Icarus 389 (2023) 115261

Contents lists available at ScienceDirect

Icarus

journal homepage: www.elsevier.com/locate/icarus

Research Paper

H_3^+ cooling in the Jovian aurora: Juno remote sensing observations and modeling

J.-C. Gérard [a,*], L. Gkouvelis [b], B. Bonfond [a], G.R. Gladstone [c,d], A. Mura [e], A. Adriani [e], D. Grodent [a], V. Hue [c], T.K. Greathouse [c]

[a] LPAP, STAR Institute, Université de Liège, Belgium
[b] NASA Ames Research Center, Moffet Field, California, USA
[c] Southwest Research Institute, San Antonio, TX, USA
[d] Physics and Astronomy Department, University of Texas at San Antonio, TX, USA
[e] Istituto di Astrofisica e Planetologia Spaziali-INAF, Rome, Italy

ARTICLE INFO

Keywords:
Jupiter
Aurorae
Ultraviolet observations
Infrared observations
Spectroscopy

ABSTRACT

Cooling of Jupiter's auroral thermosphere by H_3^+ radiation to space is one of the processes controlling the energy balance in the auroral upper atmosphere. The UltraViolet Spectrograph (UVS) and the Jupiter InfraRed Auroral Mapper (JIRAM) on board Juno have observed the Jovian polar aurora from its polar orbit since August 2016. The UVS instrument measures the H_2 Lyman and Werner bands whose brightness is a proxy of the precipitated auroral electron flux. The 3.3–3.6 μm spectral window of the JIRAM L-band imager maps the H_3^+ thermal radiance with unprecedented spatial resolution. Comparison of concurrent observations indicates that the morphological features are similar in the two spectral regions but differences are also observed in the spatial intensity contrast. We compare the total (direct and indirect) particle heating rate and the cooling by H_3^+ radiation derived from four pairs of simultaneous UVS and JIRAM images. The total auroral cooling power H_3^+ is in the range 2–4 terawatts in both hemispheres. In all cases, the H_3^+ cooling in the aurora is found to range between 0.45 and 0.67 time less than the particle collisional heating. In a second step, we use the ultraviolet H_2 brightness and FUV color ratio to derive the characteristics of the electron precipitation and model the H_3^+ radiance for each UVS map pixel. The comparison of the H_3^+ modeled radiance map with the JIRAM observations shows general good agreement with some local differences. The four spatially integrated H_3^+ cooling power from the model are in very good agreement with the JIRAM values. These results are important constraints for global magnetosphere-ionosphere-atmosphere models.

1. Introduction

The Jovian upper atmosphere is about 700 K warmer than expected from heating by solar ultraviolet radiation. Most temperature determinations in the thermosphere have been obtained from the analysis of the H_3^+ rotational distribution observed from Earth-based telescopes (Drossart et al., 1989; Lam et al., 1997; Miller et al., 1997; Stallard et al., 2002; Raynaud et al. (2004); Moore et al., 2017; Johnson et al., 2018; Migliorini et al. (2019). Temperature maps have also been made with limited spatial resolution from Juno's Jovian InfraRed Auroral Mapper (Adriani et al., 2017; Dinelli et al., 2017). Recently O'Donoghue et al. (2021) have obtained meridional cuts showing that temperatures decrease from 1000 K to 600 K between auroral latitudes and the equator. The H_3^+ ion densities are significantly increased at high latitudes as a result of auroral precipitation followed by ionization of H_2 and charge transfer, but they quickly decrease equatorward of the aurora. In contrast, temperatures remain relatively high outside the auroral regions. This moderate temperature drop-off at mid- and low latitudes has been interpreted as an indication that transport by zonal and equatorward meridional winds redistribute the auroral heat.

Ignoring heat redistribution by advection, one-dimensional models have examined the energy partition in the auroral regions. Waite et al. (1983) and Grodent et al. (2001) used a two-stream electron transport model to calculate the energy distribution of auroral electrons. For the

* Corresponding author at: LPAP, 19c allée du 6 août, B5c, Université de Liège, B-4000 Liège, Belgium.
E-mail address: jc.gerard@uliege.be (J.-C. Gérard).

https://doi.org/10.1016/j.icarus.2022.115261
Received 8 March 2022; Received in revised form 24 August 2022; Accepted 2 September 2022
Available online 11 September 2022

case of a monoenergetic 10-keV electron precipitation, Waite et al. (1983) found that the direct neutral heating by collisions amounts to 11% of the precipitated electron energy flux. They also determined that about 50% of the precipitated energy ultimately ends up as a heat source for the neutral gas. Their model simulations also indicate that 12–15% is released as H_2 Werner and Lyman band photons. Melin et al. (2006) examined the one-dimensional energy balance of the upper atmosphere during two periods when infrared spectra were collected with the IRTF facility. They combined H_3^+ intensity and ion velocity measurements to estimate the various heat sources and sinks, which led them to the conclusion that winds transport heat away from the auroral regions. Other sources include Joule and ion drag heating and adiabatic compression.

Evaluation of the relative importance of these sources including horizontal transport requires using three-dimensional Magnetosphere-Ionosphere-Thermosphere (MIT) models coupled with a global circulation model where all sources of heating, cooling and transport may be consistently estimated. A few such models have been developed. One is the Jovian Ionospheric Model (JIM) (Achilleos et al., 1998; Millward et al., 2002, 2005). The second one, the Jupiter Thermosphere General Circulation Model (JTGCM) (Bougher et al., 2005; Majeed et al., 2009) simulates the global distribution of the temperature, winds, neutrals and ions. It includes the MIT coupling by using parameterizations of ion drag and Joule heating and ion drag developed for the Earth scaled to Jupiter' characteristics. Finally, Yates et al. (2020) presented a new model coupling a Jovian 3-D GCM to a one-dimensional axisymmetric magnetosphere model.

The primary heat sinks are H_3^+ infrared radiation to space in the ionosphere named the H_3^+ thermostat by Bougher et al. (2005), infrared emission of hydrocarbons such as methane and ethylene near or below the homopause and vertical and transport by conduction and horizontal advection. The relative importance of the three processes is still largely debated. Three-dimensional model simulations have difficulties in efficiently transferring heat from high latitude to lower latitudes. One of the limitations comes from the strong Coriolis force associated with the rapid planetary rotation that creates strong zonal jets limiting efficient meridional heat transfer. For example, in Yates et al.'s (2020) model runs, the neutral temperatures in the high-latitude regions are comparable to the lower range of observed temperatures, while the modeled equatorial temperatures are still a few hundred kelvins colder than observed. In these models, Coriolis forces and possibly other processes prevent auroral energy to flow away from the polar regions, in contrast to the observations. Therefore, either there remains a still undefined mechanism that allows meridional heat transport to the equator, or another form of heating that is not included in the model is active in the equatorial region.

Concurrent observations of the Far ultraviolet observations by Hubble and ground-based infrared H_3^+ aurora have been reported by Clarke et al. (2004) and discussed by Radioti et al. (2013). They pointed out a general morphological agreement but also found that some of the emissions were not co-located in the FUV and near infrared and that the relative brightness in the two spectral bands was spatially variable and not always correlated. More recent simultaneous observations made with the UltraViolet Spectrograph (UVS) and the Jupiter InfraRed Auroral Mapper (JIRAM) instruments during the first Juno perijove pass in the north have been analyzed by Gérard et al. (2018). They also pointed out that the H_3^+ Infrared/H_2 far UV ratio varied between the different auroral components and thus that the atmospheric cooling rate by H_3^+ radiation is spatially variable relative to the incident auroral electron energy flux. However, the quantitative comparison between the sets of concurrent images was limited to two cuts across the auroral zone. They found that that in bright arcs the H_3^+ emitted infrared power was equal to 1.8 times the power emitted in the H_2 FUV emission for the first cut and 3.6 in the second cut. The ratios averaged along the full cuts were 3.4 and 7.5 for cuts 1 and 2, significantly higher than in the bright arcs. They also noticed that the highest IR/FUV ratios were coincident with regions of high FUV color ratio corresponding to zones of deeper penetration of the auroral electrons. The far UV color ratio R = I (155–162 nm)/I(123–130 nm) is the ratio between the H_2 intensity in the unabsorbed 155–162 nm range and the intensity of the partly absorbed H_2 radiation between 126 and 130 nm. It is a proxy of the energy of the auroral electrons as more energetic electrons penetrate deeper into the hydrocarbon layer, generating a stronger absorption and therefore a higher color ratio (e.g., Yung et al., 1982; Gérard et al., 2014).

In this study, we take advantage of the remote sensing instruments on board Juno that allow concurrent auroral images to be obtained in the far ultraviolet and in the infrared. Specifically, the JIRAM camera provides images of the H_3^+ radiance distribution and the UVS spectral imager maps the distribution of the H_2 ultraviolet intensity that is a good proxy of the precipitated electron flux. Similar to the 2018 study, we use simultaneous observations by UVS and JIRAM, however here we compare full images, not just cuts through the aurora, and several different perijoves with image pairs. The objective of this study is twofold:

- Take advantage of the unique extended spatial coverage provided by Juno to compare the auroral atmospheric H_2 FUV radiation from the auroral atmosphere resulting from electron precipitation with the H_3^+ radiance to space. This allows comparing the particle heat input to the neutral gas relative to the infrared cooling caused by H_3^+ infrared radiation
- Model the two-dimensional distribution of the H_3^+ radiance using UVS spectral images and compare to the JIRAM simultaneous observations. This comparison is a test of the validity of the quantitative prediction of H_3^+ cooling based on the characteristics of the electron precipitation.

In the next section, we describe the two Juno remote sensing instruments used for these comparisons, the observational constraints and the selection of the four couples of images analyzed in this study. Section 3 describes the methodology of the ultraviolet-infrared comparison of the datasets and the comparison of the H_2 FUV and H_3^+ radiances. In section 4, we present the model used to evaluate the H_3^+ radiance from the UVS spectral brightness maps and discuss the validity of the method. Conclusions about the use of FUV spectral imaging to estimates the H_3^+ cooling rate are presented in section 5.

2. Instruments and observations

Juno spins at a rate of 2 rotations per minute and carries two instruments that provide images of the polar aurora and satellite footprints. The observations reported in this study were collected with the UVS and JIRAM during the first two years of Juno operations in Jovian orbit. During this period, Juno was on a highly-elliptical 53-days orbit with a perijove at ~5000 km above the cloud top (Bolton et al., 2017). This polar orbit offers the possibility to successively observe both polar regions at distances as short as ~1 Jovian radius above the 1-bar pressure level.

UVS is a photon-counting spectrograph observing the planet every 30 s between 70 and 205 nm. This domain includes the spectral range of the H_2 Werner and Lyman bands and the Lyman-α auroral emissions. The entrance slit has a "dog-bone" shape 7.5° long. Each detector pixel has a field of view of 2.2 arcmin along the slit and 12 arcmin across. UVS is equipped with a scan mirror allowing the instrument to point ±30° from the spin plane. The spacecraft rotation produces successive stripes every ~30 s at various mirror angles that are combined to construct composite images. The disk background has been removed based on the method described by Bonfond et al. (2017). The detector count rates were converted into emitted H_2 brightness and power based on the in

board calibration using the 155–162 nm spectral region scaled up by a factor of 8.1 to get the total H_2 Lyman and Werner bands UV brightness. Images are co-added to get a nearly complete picture of the aurora in both hemispheres and projected on polar maps fixed in System III (Bonfond et al., 2017). A full description of the instrument and its operations was given by Gladstone et al. (2017). The sources of uncertainty in the count rate to brightness conversion have been discussed by Gérard et al. (2019).

For this study, we also use the data collected with the L-band JIRAM imager (Adriani et al., 2017) covering the spectral region between 3.3 and 3.6 μm that includes some of the strongest H_3^+ lines and provides good contrast against the Jovian disk. The entrance slit has a view of view of 3.5°, so that it can only cover part of the polar region in a single image during Juno's passage at perijove due to the short distance to Jupiter. However, JIRAM's field of view can be oriented with a despinning mirror to scan across most of the auroral features. These

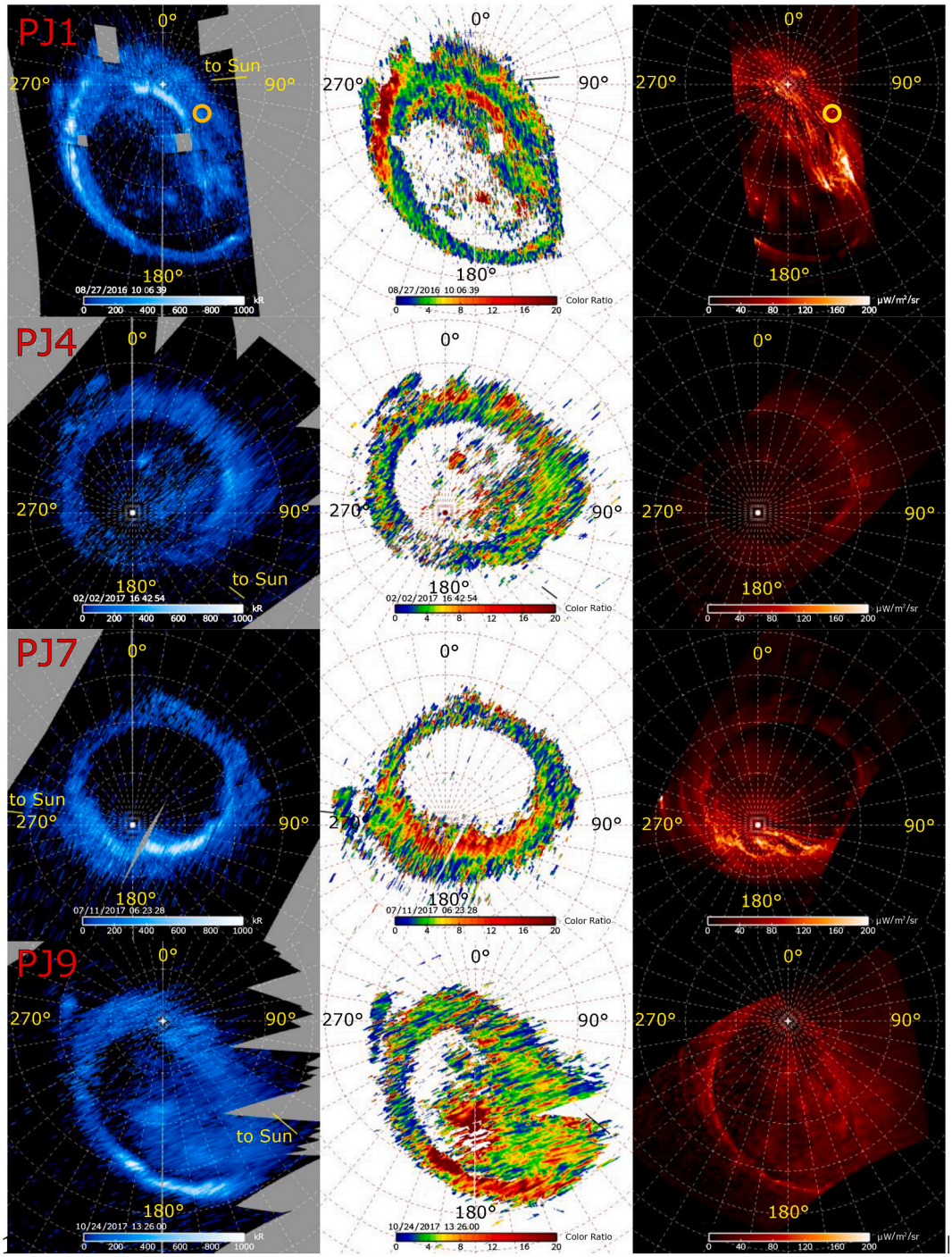

Fig. 1. polar projections of H_2 FUV, FUV color ratio and H_3^+ composite images constructed from UVS and JIRAM observations during perijoves passes of Juno orbits 1 (north), 4 (south), 7 (south) and 9 (north). Ten-degree spaced System III meridians and parallels are shown as dashed lines with System III meridians increasing clockwise every 10°. The PJ4 and PJ7 projections in the south are oriented as if the aurora was seen through the planet from above the north pole. The yellow bars on the UVS projection indicate the direction of the sun. The yellow rings in the UVS and JIRAM PJ1-N images circle the region used to produce Fig. 3. (For interpretation of the references to color in this figure legend, the reader is referred to the web version of this article.)

imaging sequences are arranged in such a way that the coverage of the main auroral region takes usually between 10 and 15 min. The images are processed and signal contamination removed as described in Mura et al. (2017, 2018). Mosaics are assembled by processing the data to remove contamination and averaging the best available data where images overlap. The combination of the uncertainty on the absolute calibration combined with the background subtraction leads to an estimated brightness error of about 20%. In contrast to UVS, JIRAM cannot observe away from the spin plane so that the field of view of the two instruments generally only partially coincides. The projection of the JIRAM H_3^+ images is made on a reference surface at 500 km. The accuracy of the localization is estimated on the order of a pixel size ≈0.8 arcmin.

In this study, we concentrate on selected periods of time when the two instruments simultaneously collected data covering a significant part of the auroral regions in the same hemisphere. Such occurrences are rather rare events since UVS collects images when overflying the polar regions while JIRAM generally operates from a farther distance from the poles to avoid contamination by energetic particles in the detector. Consequently, concurrent images with both instruments are generally obtained from rather long distances of the planet, resulting in a degraded UVS spatial resolution. A notable exception is the first perijove orbit when both UVS and JIRAM collected several nearly global auroral images.

3. Comparison of particle heating and H_3^+ cooling rates

Four cases of concurrent FUV and infrared auroral images with similar spatial coverage have been examined in detail. Polar orthographic projections of the UVS H_2 brightness, FUV color ratio and JIRAM radiance for Juno perijoves (PJ) PJ1-north, PJ4-south, PJ7-south and PJ9-north are presented in Fig. 1. The times and characteristic values related to the four observations are listed in Table 1. The UVS images correspond to the total H_2 unabsorbed brightness obtained by integrating the emission measured between 155 and 162 nm multiplied by a factor 8.1 to scale to the total intensity of the Lyman and Werner bands (Gérard et al., 2018). This method takes advantage of the negligible hydrocarbon absorption longward of ~140 nm. All auroral regions were not observed in the nadir direction. However, corresponding pixels in the two images were observed at most a few minutes apart and we consider that the difference in the viewing angle is small enough to be neglected.

We only consider those auroral areas that are common to both images in an image pair. Other regions are ignored by constructing a mask removing all pixels that are missing in at least one of the images. The next step consists of integrating the emitted radiation in both spectral ranges to determine the corresponding emitted power. The FUV power is directly derived from the integrated count rate using the most recent version of the UVS calibration (Hue et al., 2019, 2021). Similarly, the infrared radiance measured by JIRAM is spatially integrated to determine the power radiated in the 3.3–3.6 μm window. Synthetic spectra simulations assuming thermodynamic equilibrium using Dinelli et al. 's (2017) model show that the emission in this spectral domain is only weakly dependent on temperature, varying from 20.5% of the total auroral H_3^+ radiation at 800 K to 19.3% at 1000 K (Gérard et al., 2018). We adopt a value of 20% for consistency with our earlier work.

Table 1
Juno observations of concurrent UVS and JIRAM auroral images.

Perijove	start time*	H_2 power (TW)	H_3^+ power (TW)	H_3^+ cooling/ e^- heating	Model H_3^+ (TW)
PJ1-N	2016-08-27/09:54*	1.5	3.2	0.63	3.3
PJ4-S	2017-02-02/16:31	1.1	1.8	0.45	2.5
PJ7-S	2017-07-11/06:12	1.6	3.0	0.50	2.6
PJ9-N	2017-10-24/13:02	2.0	4.3	0.67	3.9

* Format is YYYY-MM-DD/HH:MM.

4. Results

For PJ1-N, the integrated H_2 emitted far ultraviolet power observed by UVS is 1464 W. The H_3^+ power measured by JIRAM is 3233 GW, that is 2.2 times the H_2 FUV emitted power. Waite et al. (1983) calculated that the gas heating rate by direct and indirect effects is equal to 3.6 times the unabsorbed energy radiated by H_2 in the far ultraviolet. Combining these two quantities, it is estimated that H_3^+ ions radiate about 63% of the gas heating rate by electron precipitation in the case of the PJ1-N image pair. Joule heating and advection also importantly contribute to heating the Jovian thermosphere. Our result indicates that atmospheric heating by the auroral electrons alone, not considering Joule and ion frictional heating, exceeds the H_3^+ cooling, confirming that radiation by hydrocarbons and transport play an important role in the heat balance of the auroral regions. We also note that the bright H_2 arc between 0° and 140° SIII longitude is relatively less pronounced in the H_3^+ emission, coincident with a high (8–15) color ratio.

The same remark applies to the bright spot at 68°, 176° S_{III} associated with a high color ratio, and also observed relatively weaker in the infrared. Other similar correlations between a high color ratio and a relatively low H_3^+/H_2 intensity ratio are also observed with the bright spots in PJ4 and the bright main emission and the polar spot present in PJ9. A similar correlation between the color ratio and the H_2/H_3+ intensity ratio was also observed for PJ1 in the intensity radial cuts described by Gérard et al. (2019). This is interpreted as a consequence of the deeper electron penetration in the methane layer where the H_3^+ ions are efficiently converted in heavier ions.

The other three cases of concurrent FUV and infrared images have been analyzed following the same procedure. The region of image PJ9-north near the limb contaminated by H_3^+ radiation from the dayside has been removed from both UV and IR images for the following numerical treatment. The integrated H_2 and H_3^+ emitted powers spatially integrated over the overlapping auroral region are listed in Table 1. In all four cases, the power radiated by H_3^+ exceeds that of FUV H_2 emitted power. Their ratio is equal to 2.2 for PJ1, 1.6 for PJ4, 1.8 for PJ7, and 2.2 for PJ9. Applying the same procedure as for PJ1-N, we find that cooling by H_3^+ is between 0.45 and 0.67 times less than heating by electron collisions (Table1). As mentioned before, this ratio is compatible with a role played by transport and hydrocarbon infrared emission as heat sinks in the heat budget of the auroral upper atmosphere to eliminate the excess heat production.

5. Atmospheric cooling by H_3^+ radiation

We briefly describe the model used to calculate the H_3^+ auroral cooling rate based on the characteristics of the electron precipitation remotely determined from the ultraviolet spectral images (Gérard et al., 2020). We first determine the H_2 brightness on each UVS pixel in the unabsorbed 155–162 nm spectral window. The value is scaled up by 8.1 to obtain the total FUV brightness in the H_2 Lyman and Werner bands. The corresponding electron energy flux is based on an efficiency factor of ~10 kR of H_2 FUV emission corresponding to a precipitated electron energy flux of 1 mW m^{-2}, as discussed by Gérard et al. (2019, Appendix). The FUV color ratio of the pixel is used to estimate the mean electron energy following the procedure described by Gérard et al. (2020). The neutral atmospheric model is taken from Grodent et al. (2001). Using the precipitated electron energy flux and mean electron energy, the H_2 ionization rate along the electron path is calculated using Hiraki and Tao's (2008) parameterization. H_2^+ ions efficiently transfer

their charge to ambient H_2 molecules and create H_3^+ ions. These, in turn, transfer charge to heavier carbonated ions in the lower ionosphere near and below the homopause. In this way, the steady state H_3^+ ion density profile is obtained between 200 and 2500 km altitude in all auroral pixels. The next step consists in calculating the H_3^+ cooling rate as a function of altitude. For this, we use the results of the model by Miller et al. (2013) who provided calculations of the H_3^+ cooling per ion E(H_3^+) for a range of temperatures and H_2 densities. This model includes the non-LTE effects in conditions when the H_2 density becomes too low to ensure that the population of the excited levels is fully controlled by collisions. The consequence is that even though the temperature increases with altitude in the Jovian thermosphere, the cooling efficiency decreases at high altitudes where collisions become rare and radiation relatively inefficient. Miller et al. (2013) have calculated polynomial expressions for the cooling function together with scaling factors depending on the H_2 density to account for the non-LTE corrections. We have adopted their values to determine the altitude distribution of the H_3^+ cooling rate per unit volume. Once this altitude profile is available for each UVS pixel, the local cooling is directly obtained by vertical integration as optical depth effects are negligible even in the auroral regions (Lam et al., 1997).

The use of a fixed vertical temperature distribution is a limitation to the accuracy of the determination of the H_3^+ cooling rate. The infrared volume emission rate under thermodynamic equilibrium depends linearly on the H_3^+ density and exponentially on temperature (Johson et al., 2018). However, a strong correlation was found between the H_3^+ emission and its column density by Stallard et al. (2002), Moore et al. (2017), Adriani et al. (2017) and Johson et al. (2018). This correlation implies that the ionization rate efficiently controls the H_3^+ cooling rate. Since only a modest correlation was observed between H_3^+ emission and temperature, Johson et al. (2018) concluded that temperature is only a second driver of H_3^+ emission, less important than the H_3^+ column density.

The Grodent et al. (2001) temperature profile compares favorably with ultraviolet and infrared auroral observations but local departures from this distribution are expected, depending on the strength and history of the electron precipitation. As a sensitivity test, the H_3^+ cooling rate has been calculated using temperature and neutral atmospheric density distributions for the three widely different T(z) profiles. They correspond to exospheric temperatures of 440 K (case A), 600 K (case B) and 940 K (case C). Fig. 2 shows the vertical distribution of the H_3^+ density for these three cases. All three curves are calculated for an auroral precipitation characterized by a H_2 unabsorbed nadir intensity of 100 kR (electron energy flux of 10 mW m^{-2}), a FUV color ratio of 5 and a local magnetic field of 10 nT. They show that the density peak values are quite similar but the vertically integrated column densities vary from 6.4×10^{11} to 8.8×10^{11} cm^{-2} between cases A and case C. The associated H_3^+ cooling power increases by a factor of 1.4, in the same ratio as the H_3^+ column densities.

In the absence of temperature determination in each pixel, we use the T(z) vertical distribution from Grodent et al. (2001) for all pixels. Fig. 3 shows an example of altitude distribution of the particle heating and the calculated H_3^+ cooling power for a group of 3 × 3 pixels located at 82° N and 125° S_{III} longitude where the H_2 FUV FUV brightness is 225 kR The vertical distribution of the heating rate by auroral electrons is calculated by the electron transport model while the H_3^+ cooling is obtained as described before. The peak value of the H_3^+ radiated power is in close agreement with the value calculated by Melin et al. (2006) but our profile has a sharper peak. This difference mostly stems from their extended distribution of the energy of the auroral electrons (scaled from Grodent et al., 2004) compared to our monoenergetic precipitation. The peak altitudes of the electron heating and H_3^+ cooling are 310 and 380 km respectively.

The offset of the peak of the H_3^+ power relative to the electron heating is a consequence of the loss of H_3^+ ions near and below the homopause following their reaction with CH_4. The topside scale height of the H_3^+ cooling is larger than that of the heating, caused by the slower decrease of the H_3^+ density compared to the heating rate.

6. Results

We now compare the total auroral H_3^+ cooling power simulated by the model and the JIRAM observations. The calculated values for the four perijoves are listed in the last column of Table 1. In the case of PJ1-N, the highest quality concurrent set of FUV and infrared observations. The calculated total power is 3348 GW, to be compared with the 3291 GW from the JIRAM observations. The relative difference is thus about 4%, well within the uncertainties of the measurements and the model. The differences for the other three sets of simultaneous IR and FUV images listed in Table 1 are 39%, 14% and 26%, that is remarkably close to each other considering uncertainties from the absolute calibration of the instrument and the removal of signal contamination.

The map of the calculated H_3^+ cooling rate corresponding to the PJ1-N images in Fig. 1a is shown in Fig. 4, together with that observed by JIRAM. The main morphological features are similar with two bright regions located near the pole between 30° and 50° N and between 310° and 330° S_{III} longitudes. Similarly, another bright H_3^+ feature is observed in both projections at 70° N and 160° S_{III} longitude.

A segment of the main emission between 50° and 60° N is clearly

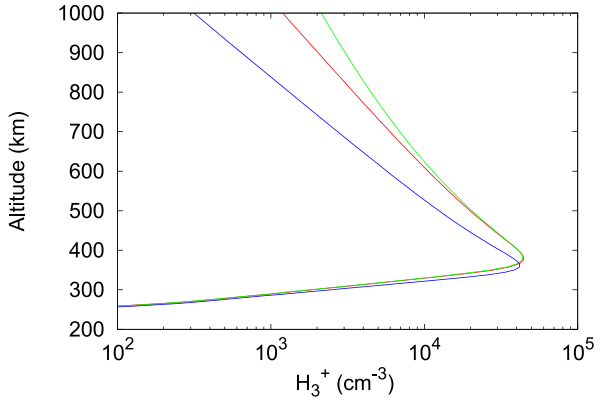

Fig. 2. calculated H_3^+ density distribution for three different temperature and neutral density models. The blue curve corresponds to case A, red to case B and green to case C (see text). (For interpretation of the references to color in this figure legend, the reader is referred to the web version of this article.)

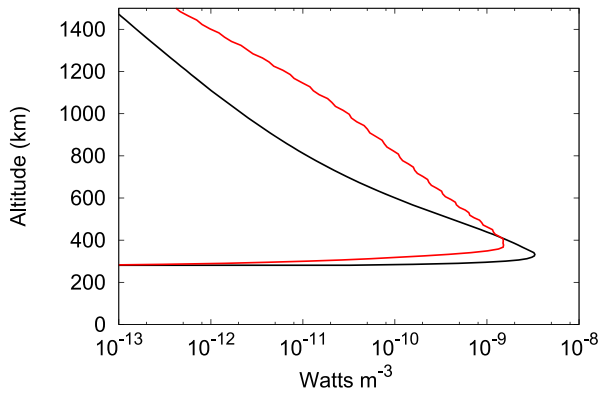

Fig. 3. example of calculated electron heating (in black) and H_3^+ radiated power (in red) for the location circled on the UVS PJ1-N image in Fig. 1 (see text). (For interpretation of the references to color in this figure legend, the reader is referred to the web version of this article.)

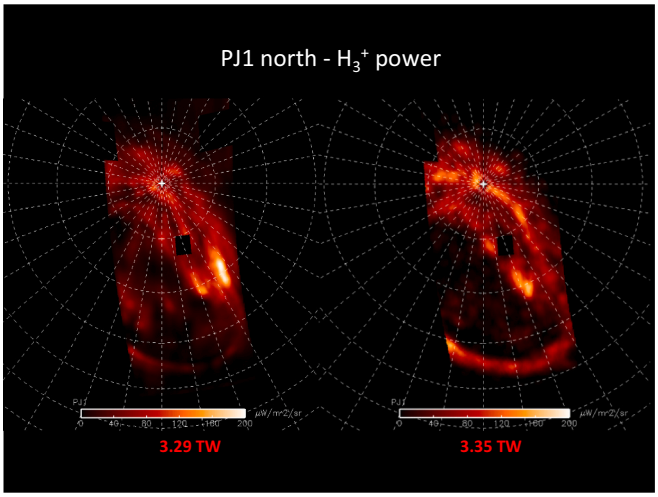

Fig. 4. left: smoothed H_3^+ cooling rate from JIRAM reconstructed image during the PJ1-N perijove (Fig. 1a); right: calculated H_3^+ cooling rate based on the UVS concurrent image (see text). Both polar projections are smoothed over a distance of 2000 km. The spatially integrated cooling rates are indicated in terawatt.

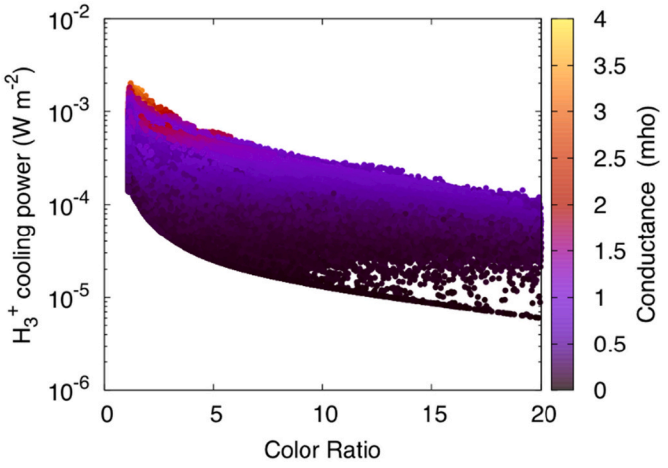

Fig. 5. H_3^+ cooling power determined for each pixel of the PJ1 JIRAM image versus its corresponding FUV color ratio. The Pedersen conductance of each pixel is given according to the color scale on the right.

apparent between 150° and 190° longitude in both maps. Differences between the two maps mainly concern the relative intensity of several auroral regions. For example, the bright spot observed by JIRAM around 70° N, 144° S_{III} does not appear in the calculated cooling map although it is brighter than its neighbor spot in the JIRAM observations. Also, the diffuse H_3^+ polar emissions inside the main oval appear weaker in the model map than in the observations. These differences are possibly partly due to differences in temporal variations between the H_2 emission that promptly follows changes in the electron precipitation and the H_3^+ radiation somewhat lagging behind them. In addition, both images are constructed by combining a mosaic of swaths collected independently, so that a given location may be imaged several minutes apart by the two instruments. We also note that both regions are characterized by a high FUV color ratio value (close to 20). Consequently, a substantial part of the modeled electron beam penetrates near and below the homopause where the produce H_3^+ ions that are rapidly converted into $C_2H_2^+$ and heavier hydrogenated ions by reaction with methane and do not contribute to H_3^+ emission. The efficiency of this conversion may be locally over- our underestimated in the model simulation.

The role of methane in the H_3^+ destruction and consequent decrease of the heating rate when the peak altitude of the aurora decreases is illustrated in Fig. 5 for the case of Juno's first orbit (PJ1 north). Each pixel is represented by its FUV color ratio and H3+ cooling power determined from the JIRAM image. It shows that when the FUV color ratio increases, H_3^+ is converted into heavier ions (as indicated by high color ratios) and the cooling rate tends to decrease. This behavior is in agreement with the destruction of H_3^+ ions when an increasing fraction is lost by reaction with methane. For sake of completeness, the color-coded Pedersen conductance calculated following the method described by Gérard et al. (2020) is also presented for each pixel.

7. Discussion and conclusions

7.1. Energy balance

Melin et al.'s (2006) one-dimensional model of the thermal balance in the aurora combined ground-based high-resolution measurements of the H_3^+ line intensities and velocities with a vertical model of the Jovian upper atmosphere and thermosphere including downward conduction and H_3^+ radiation to space. They estimated that Joule heating combined with ion drag heating exceeds particle heating by a factor of about ~6 in a vertical column. Cooling by hydrocarbons (mainly methane) was found dominant near and below the homopause and is nearly equal to Joule and ion drag heating and about 13 times the H_3^+ radiative cooling. Johnson et al. (2018) presented high spatial resolution maps of the H_3^+ emission, column density and temperature in the northern aurora. They showed that the correlation between the H_3^+ auroral temperature and its column density is modest and concluded that other processes than heating by particle impact such as Joule heating must also be playing a role. A similar result was obtained from JIRAM observations performed during the first Juno perijove by Adriani et al. (2017). From the weak correlation between temperature and H_3^+ column, they deduced that particle impact is not the major source of gas heating. They concluded that the heating mechanisms that control the Jovian thermospheric temperature are not simple.

Majeed et al. (2009) showed that the JTGCM predicts that at high altitude above the 1 nbar level in the main aurora, particle heating is dominant followed by Joule heating, but that Joule and adiabatic heating dominates at altitudes above the 1 μbar level. Cooling below the 1-μbar level is dominated by advection and mid-infrared cooling. Using their coupled MIT-GCM coupled model, Yates et al. (2020) found that magnetospheric power, Joule and ion drag heating make similar global contributions in the northern hemisphere.

These studies lead to the conclusion that heating of the neutral gas by auroral particle impact is only one, perhaps minor, component of the total heat budget. Similarly, cooling by H_3^+ radiation to space competes with horizontal winds and conduction to lower altitude, where thermal hydrocarbon emissions become important as loss sources. In these conditions, it is not possible to calculate a full energy balance in the aurora solely based on the Juno remote sensing data. However, our estimated particle heating and H_3^+ cooling rates are important constraints on global magnetosphere-ionosphere-atmosphere models to validate these measurable quantities. In particular, the H_3^+ density and the associated infrared radiation may be calculated using the same approach as described here and compared with the values given in this study.

7.2. H_3^+ cooling

The results presented in section 3.1 indicate that cooling by H3+ infrared radiation shows a morphology that closely resembles the pattern of the auroral cooling derived from the FUV spectral images. Detailed comparisons show that local in morphology and relative

brightness of some regions are also observed. They may be at least partly explained by uncertainties on and the variability of the methane distribution in the auroral regions. These uncertainties impact both the determination of the mean electron energy based on the FUV color ratio and the efficiency of the conversion of H3+ ions to carbonated ions following the H3+ + CH4 reaction in regions of deeper penetration of the auroral more energetic electrons. Another likely source of local differences stems from the used of a fixed temperature distribution. Observations (Raynaud et al., 2004; Johson et al., 2018) have shown temperature differences along the main emission. For example, the higher temperature shown in Johnson et al.'s Fig. 3 possibly explains why the calculated cooling power in the bottom left of our Fig. 4 is less than the JIRAM observations. Similarly, the cooler region observed by Johnson et al., (2018) may account for the overestimate of the calculated powers in the middle right of our calculated map. Nevertheless, we note that when integrated over the auroral regions (Table 1), calculations of the infrared cooling based on the FUV spectral images closely match the JIRAM observations in both polar regions.

The H_3^+ power derived from JIRAM images may be compared with earlier estimates. Lam et al. (1997) estimated the integrated H_3^+ emission from ground–based spectral observations with the UKIRT telescope on Mauna Kea. They obtained power values equal to 3.4 TW in the north and 3.0 TW in the south. These values are compatible with those observed with JIRAM and predicted by our model shown in Table 1.

Closing of the local energy balance in each pixel at all altitudes would require additional observational contraints. These mostly concern the heating and cooling terms in the heat equation that are not available in this study that is entirely based on ultraviolet and infrared remote sensing data collected by instruments on board Juno. In particular, Joule and ion friction heating appear to play an important role. Their evaluation would require combining the Perdersen electrical conductivity profile (which we can deduce from the FUV spectral images) with the distribution of the electric field in the ionosphere. The latter quantity can currently be derived from three-dimensional model calculations including magnetosphere-ionosphere-thermosphere coupling. Horizontal and vertical transport equally play an important role in the control of the thermospheric temperature as was demonstrated by general circulation models and recent measurements of the latitudinal temperature gradient by O'Donoghue et al. (2021). A difficulty here is that current GCMs cannot model the efficient latitudinal heat transport from the auroral regions to the lower latitudes and thus realistically globally redistribute the auroral heat over the planet. Ultimately, a combination of 3-D MIT-GCM models with measured heat and cooling terms such as derived in this study would be an efficient tool to understand the global energy balance of the Jovian upper atmosphere.

Data availability statement

JIRAM data used in this study is publicly available on the Planetary Data System (http://pds.nasa.gov) and can be downloaded from http://atmos.nmsu.edu:8080/pds. The individual datasets are available at https://atmos.nmsu.edu/ PDS/data/jnojir_xxxx, where xxxx is 1001, 1002, or 1003 for EDR (Experiment Data Record; raw data) and 2001, 2002, or 2003 for RDR (Reduced Data Record; calibrated data) volumes.

Similarly, the Juno UVS/Juno calibrated data used in this study are publicly available on the PDS NASA site and are available from https://pds-atmospheres.nmsu.edu/data_and_services/atmospheres_data/JUNO/uvs.html#Calibrated.

Declaration of Competing Interest

The authors declare the following financial interests/personal relationships which may be considered as potential competing interests: no financial interest or personal relationships.

Data availability

Data will be made available on request.

Acknowledgements

B. B. is a Research Associate of the Belgian Fonds de la Recherche Scientifique-FNRS. J.C.G., B. B. and D.G. and acknowledge financial support from the Belgian Federal Science Policy Office (BELSPO) via the PRODEX Program of ESA. L.G. was supported by an appointment to the National Aeronautics and Space Administration (NASA) Postdoctoral Program at the Ames Research Center administrated by the Universities Space Research Association (USRA) through a contract with NASA. We are grateful to NASA and contributing institutions that have made the Juno mission possible. This work was funded by NASA's New Frontiers Program for Juno via contract with the Southwest Research Institute. The JIRAM instrument was supported by the Italian Space Agency through ASI-INAF contracts I/010/10/0 and 2014-050-R.0.

References

Achilleos, N., Miller, S., Tennyson, J., Aylward, A.D., Mueller-Wodarg, I., Rees, D., 1998. JIM: a time-dependent, three-dimensional model of Jupiter's thermosphere and ionosphere. J. Geophys. Res. Planets 103 (E9), 20089–20112.

Adriani, A., Mura, A., Moriconi, M.L., Dinelli, B.M., Fabiano, F., Altieri, F., et al., 2017. Preliminary JIRAM results from Juno polar observations: 2. Analysis of the Jupiter southern H_3^+ emissions and comparison with the north aurora. Geophys. Res. Lett. 44, 4633–4640. https://doi.org/10.1002/2017GL072905.

Bolton, S.J., Lunine, J., Stevenson, D., Connerney, J.E.P., Levin, S., Owen, T.C., et al., 2017. The Juno mission. Space Sci. Rev. 213 (1–4), 5–37.

Bonfond, B., Gladstone, G.R., Grodent, D., Greathouse, T.K., Versteeg, M.H., Hue, V., et al., 2017. Morphology of the UV aurorae Jupiter during Juno's first perijove observations. Geophys. Res. Lett. 44 (10), 4463–4471.

Bougher, S.W., Waite, J.H., Majeed, T., Gladstone, G.R., 2005. Jupiter Thermospheric general circulation model (JTGCM): global structure and dynamics driven by auroral and Joule heating. J. Geophys. Res. Planets 110, E04008.

Clarke, J.T., Grodent, D., Cowley, S.W., Bunce, E.J., Zarka, P., Connerney, J.E., Satoh, T., 2004. Jupiter's aurora. Jupiter 1, 639–670.

Dinelli, B.M., Fabiano, F., Adriani, A., Altieri, F., Moriconi, M.L., Mura, A., Olivieri, A., 2017. Preliminary JIRAM results from Juno polar observations: 1. Methodology and analysis applied to the Jovian northern polar region. Geophys. Res. Lett. 44 (10), 4625–4632.

Drossart, P., Maillard, J.P., Caldwell, J., Kim, S.J., Watson, J.K.G., Majewski, W.A., Wagener, R., 1989. Detection of H_3^+ on Jupiter. Nature 340 (6234), 539–541.

Gérard, J.C., Bonfond, B., Grodent, D., Radioti, A., Clarke, J.T., Gladstone, G.R., Shematovich, V.I., 2014. Mapping the electron energy in Jupiter's aurora: Hubble spectral observations. J. Geophys. Res. Space Physics 119 (11), 9072–9088.

Gérard, J.C., Mura, A., Bonfond, B., Gladstone, G.R., Adriani, A., Hue, V., Levin, S.M., 2018. Concurrent ultraviolet and infrared observations of the north Jovian aurora during Juno's first perijove. Icarus 312, 145–156.

Gérard, J.C., Bonfond, B., Mauk, B.H., Gladstone, G.R., Yao, Z.H., Greathouse, T.K., et al., 2019. Contemporaneous observations of Jovian energetic auroral electrons and ultraviolet emissions by the Juno spacecraft. J. Geophys. Res. Space Physics 124, 8298–8317. https://doi.org/10.1029/2019ja026862.

Gérard, J.C., Gkouvelis, L., Bonfond, B., Grodent, D., Gladstone, G.R., Hue, V., et al., 2020. Spatial distribution of the Pedersen conductance in the Jovian aurora from Juno-UVS spectral images. J. Geophys. Res. 125, e2020JA028142 https://doi.org/10.1029/2020JA028142.

Gladstone, G.R., Persyn, S.C., Eterno, J.S., Walther, B.C., Slater, D.C., Davis, M.W., Denis, F., 2017. The ultraviolet spectrograph on NASA's Juno mission. Space Sci. Rev. 213 (1), 447–473.

Grodent, D., Waite Jr., J.H., Gérard, J.C., 2001. A self-consistent model of the Jovian auroral thermal structure. J. Geophys. Res. Space Physics 106 (A7), 12933–12952.

Hiraki, Y., Tao, C., 2008. Parameterization of ionization rate by auroral electron precipitation in Jupiter. Ann. Geophys. 26, 77–86. https://doi.org/10.5194/angeo-26-77-2008.

Hue, V., Gladstone, G.R., Greathouse, T.K., Kammer, J.A., Davis, M.W., Bonfond, B., Byron, B.D., 2019. In-flight characterization and calibration of the Juno-ultraviolet spectrograph (Juno-UVS). Astron. J. 157 (2), 90.

Hue, V. Rohini, Giles, S., Gladstone, George R., Greathouse, Thomas K., Davis, Michael W., Kammer, Joshua A., Versteeg, Maarten H., 2021. Updated radiometric and wavelength calibration of the Juno ultraviolet spectrograph. J. Astron. Telesc. Instrum. Syst. 7 (4), 044003 https://doi.org/10.1117/1.JATIS.7.4.044003.

Johnson, R.E., Melin, H., Stallard, T.S., Tao, C., Nichols, J.D., Chowdhury, M.N., 2018. Mapping H_3^+ temperatures in Jupiter's northern Auroral ionosphere using VLT-CRIRES. J. Geophys. Res. Space Physics 123 (7), 5990–6008.

Lam, H.A., Achilleos, N., Miller, S., Tennyson, J., Trafton, L.M., Geballe, T.R., Ballester, G.E., 1997. A baseline spectroscopic study of the infrared aurorae of Jupiter. Icarus 127, 379–393.

Majeed, T., Waite, J.H., Bougher, S.W., Gladstone, G.R., 2009. Processes of auroral thermal structure at Jupiter: analysis of multispectral temperature observations with the Jupiter thermosphere general circulation model. J. Geophys. Res. Planets 114 (E7).

Melin, H., Miller, S., Stallard, T., Smith, C., Grodent, D., 2006. Energy balance in the Jovian atmosphere during an auroral heating event. Icarus 181, 256–265.

Migliorini, A., Dinelli, B.M., Moriconi, M.L., Altieri, F., Adriani, A., Mura, A., Plainaki, C., 2019. H_3^+ characteristics in the Jupiter atmosphere as observed at limb with Juno/JIRAM. Icarus 329, 132–139.

Miller, S., Achilleos, N., Ballester, G.E., Lam, H.A., Tennyson, J., Geballe, T.R., Trafton, L. M., 1997. Mid-to-low latitude H_3^+ emission from Jupiter. Icarus 130 (1), 57–67.

Miller, S., Stallard, T., Tennyson, J., Melin, H., 2013. Cooling by H_3^+ emission. J. Phys. Chem. 117, 9770–9777.

Millward, G., Miller, S., Stallard, T., Aylward, A.D., Achilleos, N., 2002. On the dynamics of the Jovian ionosphere and thermosphere III. The modelling of auroral conductivity. Icarus 160, 95–107. https://doi.org/10.1006/icar.2002.6951.

Millward, G., Miller, S., Stallard, T., Achilleos, N., Aylward, A.D., 2005. On the dynamics of the Jovian ionosphere and thermosphere. IV. Ion-neutral coupling. Icarus 173, 200–211. https://doi.org/10.1016/j.icarus.2004.07.027.

Moore, L., O'Donoghue, J., Melin, H., Stallard, T., Tao, C., Zieger, B., Bolton, S., 2017. Variability of Jupiter's IR H_3^+ aurorae during Juno approach. Geophys. Res. Lett. 44 (10), 4513–4522.

Mura, A., Adriani, A., Altieri, F., Connerney, J.E.P., Bolton, S.J., Moriconi, M.L., Olivieri, A., 2017. Infrared observations of Jovian aurora from Juno's first orbits: main oval and satellite footprints. Geophys. Res. Lett. 44 (11), 5308–5316.

Mura, A., Adriani, A., Connerney, J.E.P., Bolton, S., Altieri, F., Bagenal, F., Turrini, D., 2018. Juno observations of spot structures and a split tail in Io-induced aurorae on Jupiter. Science 361 (6404), 774–777.

O'Donoghue, J., Moore, L., Bhakyapaibul, T., Melin, H., Stallard, T., Connerney, J.E.P., Tao, C., 2021. Global upper-atmospheric heating on Jupiter by the polar aurorae. Nature 596 (7870), 54–55.

Radioti, A., Lystrup, M., Bonfond, B., Grodent, D., Gérard, J.C., 2013. Jupiter's aurora in ultraviolet and infrared: simultaneous observations with the Hubble space telescope and the NASA infrared telescope facility. J. Geophys. Res. Space Physics 118 (5), 2286–2295.

Raynaud, E., Lellouch, E., Maillard, J.P., Gladstone, G.R., Waite Jr., J.H., Bézard, B., Fouchet, T., 2004. Spectro-imaging observations of Jupiter's 2-μm auroral emission. I. H_3^+ distribution and temperature. Icarus 171 (1), 133–152.

Stallard, T., Miller, S., Millward, G., Joseph, R.D., 2002. On the dynamics of the Jovian ionosphere and thermosphere: II. The measurement of H_3^+ vibrational temperature, column density, and total emission. Icarus 156 (2), 498–514.

Waite, J.H., Cravens, T.E., Kozyra, J., Nagy, A.F., Atreya, S.K., Chen, R.H., 1983. Electron precipitation and related aeronomy of the Jovian thermosphere and ionosphere. J. Geophys. Res. Space Physics 88, 6143–6163.

Yates, J.N., Ray, L.C., Achilleos, N., Witasse, O., Altobelli, N., 2020. Magnetosphere–ionosphere–thermosphere coupling at Jupiter using a three-dimensional atmospheric general circulation model. J. Geophys. Res. Space Physics 125, e2019JA026792. https://doi.org/10.1029/2019JA026792.

Yung, Y.L., Gladstone, G.R., Chang, K.M., Ajello, J.M., Srivastava, S.K., 1982. H_2 fluorescence spectrum from 1200 to 1700 a by electron impact - laboratory study and application to Jovian aurora. Astrophys. J. Lett. 254, L65–L69. https://doi.org/10.1086/183757.